Geochimica et Cosmochimica Acta, Vol. 69, No. 10, pp. 2663–2674, 2005

0016-7037/05 $30.00 + .00

doi:10.1016/j.gca.2004.12.005

Correlations between oxygen-isotopic composition and petrologic setting in a coarse-grained Ca, Al–rich inclusion

MIWA YOSHITAKE,[1,*,‡] YOSHIYUKI KOIDE,[2,†] and HISAYOSHI YURIMOTO[1,**]

[1]Department of Earth and Planetary Sciences, Tokyo Institute of Technology, Meguro, Tokyo 152-8551, Japan
[2]Kanagawa Prefectural Museum of National History, 499 Iriuda, Odawara, Kanagawa 250, Japan

(*Received April* 30, 2004; *accepted in revised form December* 8, 2004)

Abstract—Oxygen-isotopic compositions in conjunction with petrologic investigation have been determined for a coarse-grained type B2 Ca, Al–rich inclusion (CAI) from the reduced CV3 Vigarano using secondary ion mass spectrometry. The oxygen-isotopic compositions of minerals are distributed along the carbonaceous chondrite anhydrous mineral line indicating mixing between ^{16}O-rich and ^{16}O-poor nebular components. The O-isotopic heterogeneities among and within minerals in the CAI interior indicate that CAI formation started in an ^{16}O-rich nebula and subsequently continued in an ^{16}O-poor nebula. ^{16}O-rich signatures of melilite and fassaite in the Wark-Lovering rim and of olivine of the accretionary rim indicate that the nebular environment during formation of the CAI returned to an ^{16}O-rich composition after processing in an ^{16}O-poor nebula. These O-isotopic variations in the CAI support multiple heating events in the solar nebula and indicate that the nebular environments fluctuated from ^{16}O-rich to ^{16}O-poor and back to ^{16}O-rich compositions during the formation of a single CAI. *Copyright © 2005 Elsevier Ltd*

1. INTRODUCTION

It is believed that at least two distinct oxygen-isotope reservoirs existed in the solar nebula (Clayton, 1993). One of the reservoirs resembles, but is not identical to, the O-isotopic composition of the Earth, and another is enriched in ^{16}O relative to the Earth by 4% (Clayton, 1993) to 8% (Kobayashi et al., 2003). The O-isotopic compositions of materials in the solar system can be derived by mixing of the two reservoirs and mass-dependent isotope fractionation (Clayton, 1993); the only exception is presolar grains (Nittler, 2003; Messenger et al., 2003; Nagashima et al., 2004; Nguyen and Zinner, 2004). These two reservoirs cannot be derived from each other by mass-dependent isotope fractionation. Isotope fractionation processes not depending on the mass differences (mass-independent isotope fractionation) in nature are not fully understood. Therefore, the origin of these two reservoirs is still controversial, but several processes have been proposed, including: nucleosynthesis (Clayton, 1993), isotopic symmetry effects (Thiemens, 1999), and self-shielding effects (Thiemens and Heidenreich, 1983; Kitamura and Shimizu, 1983; Clayton, 2002; Yurimoto and Kuramoto, 2002, 2004; Lyons and Young, 2004).

Ca, Al–rich inclusions (CAIs) are believed to have been formed initially in an ^{16}O-rich solar nebula followed by processing in an ^{16}O-poor solar nebula based on the occurrence of ^{16}O-rich spinel and ^{16}O-poor melilite within a single CAI (Clayton, 1993). This environmental change from an ^{16}O-rich to an ^{16}O-poor nebula was directly demonstrated by a melilite single crystal having O-isotopic zoning, with an ^{16}O-rich core surrounded by an ^{16}O-poor rim (Yurimoto et al., 1998). On the other hand, the opposite trend of O-isotopic compositional change in the nebula (i.e., from ^{16}O-poor to ^{16}O-rich) has been recently found in a CAI (Itoh and Yurimoto, 2003). The presence of ^{16}O-rich Wark-Lovering rims (Wark and Lovering, 1977) and accretionary rims (Hiyagon, 1998; McKeegan et al., 1998; Cosarinsky et al., 2001, 2002; Krot et al., 2002) support this opposite trend. Combining this evidence, O-isotopic compositions of the gas in the CAI-forming region seem to have changed not monotonically but cyclically. A possible setting of the cyclic O-isotopic variations has been proposed as flare heating at the inner edge of a fluctuating gas disk coupled with protosun activities (Yurimoto et al., 2001; Itoh and Yurimoto, 2003).

An alternative mechanism for O-isotopic exchange of CAI minerals is by aqueous alteration on the chondrite parent body (Ash and Young, 2000; Wasson et al., 2001; Imai and Yurimoto, 2003; Itoh et al., 2004). This parent body process is effective for fine-grained CAIs but less effective for coarse-grained CAIs (Fagan et al., 2004a). However, O-isotopic exchange in the nebula has also been proposed for fine-grained CAIs (Aléon et al., 2002; Itoh and Yurimoto, 2003; Fagan et al., 2004b). O-isotopic exchange from ^{16}O-poor to ^{16}O-rich does not occur by parent body processes.

Here we report mineralogic, petrographic, and O-isotopic studies of individual minerals of the interior, Wark-Lovering rim, and accretionary rim of a type B2 CAI in a member of the reduced subgroup of CV3 chondrites, Vigarano. Although numerous precise studies have been made in coarse-grained CAIs from the Allende oxidized CV3 chondrite, the CAIs undergo severe aqueous alterations on the parent body. The degree of alteration is smaller in reduced CV chondrites than oxidized CV chondrites (Krot et al., 2000). Therefore, to study oxygen-isotopic evolution of the solar nebula, coarse-grained CAIs from reduced CV3 chondrites are one of the best objects among chondrites. This is the first report of the O-isotopic composition of melilite in a Wark-Lovering rim.

* Author to whom correspondence should be addressed (miwa@geo.titech.ac.jp).
‡ *Present address:* Department of Earth and Planetary Sciences, Hokkaido University, Sapporo 060-0810, Japan.
† *Present address:* Department of Social Information, Sapporo Gakuin University, 11-banch Bunkyodai, Ebetsu, Hokkaido 059-8555, Japan.
** *Present address:* Department of Earth and Planetary Sciences, Kobe University, 1-1 Rokkodai-cho, Nada, Kobe 657-8501, Japan.

2. EXPERIMENTAL PROCEDURES

2.1. Sample Preparation and Petrographic and Chemical Analysis

A thick section of Vigarano, containing a coarse-grained CAI (TTV1-01), was coated with a 30-nm-thick carbon film for electron microscopy. The petrologic and mineralogic studies of the CAI were executed with a JEOL JSM-5310LV scanning electron microscope, equipped with an energy-dispersive X-ray spectrometer, Oxford LINK ISIS, at Tokyo Institute of Technology (TiTech SEM-EDS system). Backscattered electron images and quantitative chemical analyses were obtained with this system. X-ray intensities for elements were collected at an accelerating voltage of 15 keV and beam currents of ~1 nA for quantitative analysis. The measurement time for each point was set to 100 s. The X-ray data were corrected to quantitative values by an Oxford-supplied ZAF method.

2.2. Oxygen-Isotope Analysis

O-isotopic compositions of individual minerals were measured by secondary ion mass spectrometry (SIMS), using the TiTech CAMECA ims 1270, with a high mass resolution technique. The primary ion beam was mass-filtered $^{133}Cs^{+}$ ions accelerated to 20 keV. The beam spot size was ~3 μm in diameter. The typical primary current was 2 pA and was adjusted to obtain a count rate of negative secondary ^{16}O ions of 4×10^5 cps for each measurement. A normal-incident electron gun was used for charge compensation of the analysis area.

Negative secondary ions of the ^{16}O-tail, ^{16}O, ^{17}O, ^{16}OH, and ^{18}O

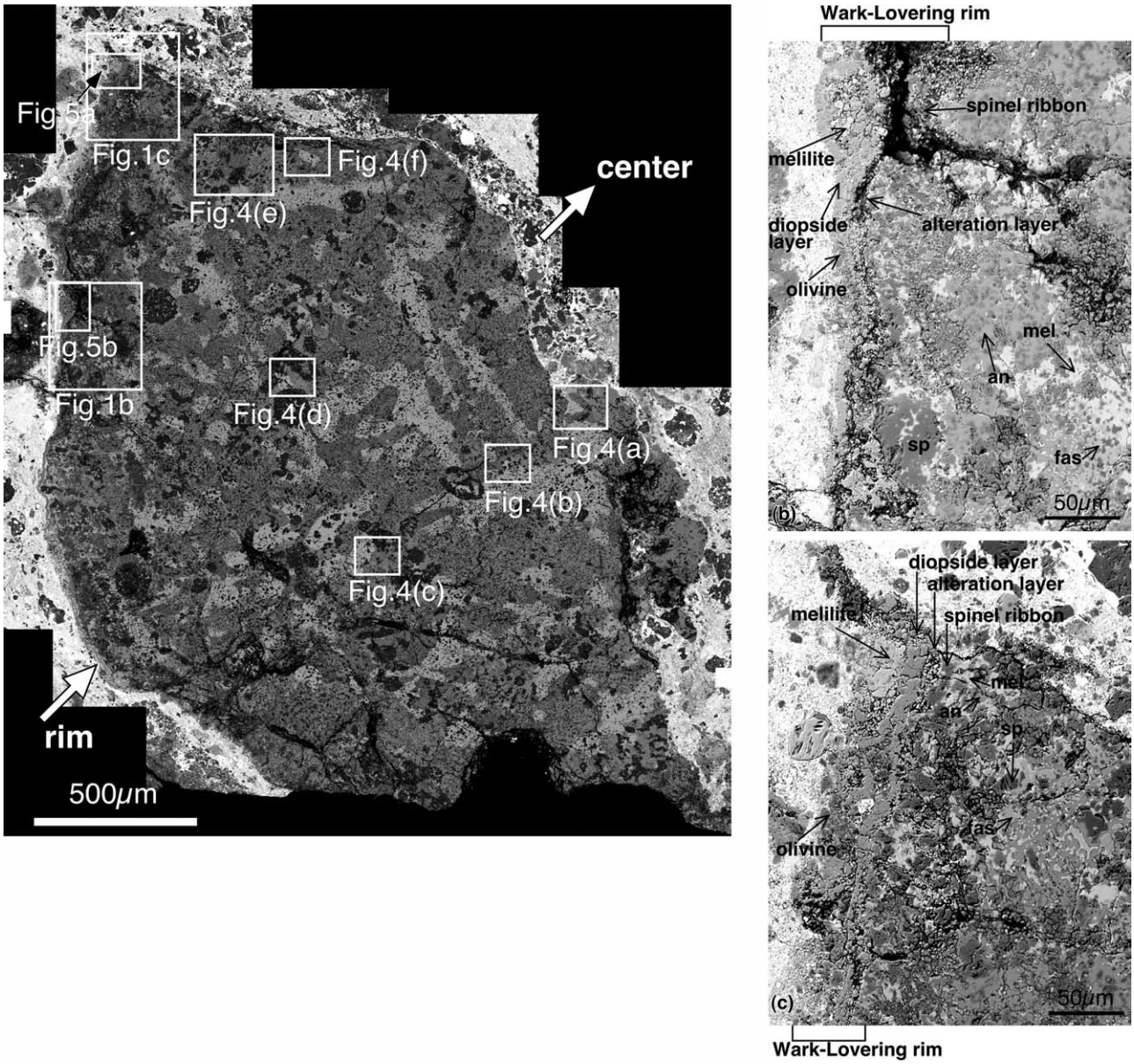

Fig. 1. Backscattered electron images of TTV1-01, type B2 CAI from the Vigarano meteorite. (a) Whole image. Magnified images of white squares are shown in Figures 1b and c, 4, and 5. Arrows show a position of rim and the direction toward the center of the CAI. (b, c) Backscattered electron images of Wark-Lovering rim and accretionary rim of TTV1-01. Melilite in a pocket of diopside layer is observed in (b). Melilite outside of diopside layer is observed in (c).

Table 1. Representative chemical compositions (weight %) of minerals in TTV1-01.

Mineral	spinel					
Position	center	center	center	center	margin	margin
MgO	26.9	27.3	28.1	28.4	26.8	23.4
Al_2O_3	69.5	71.2	71.7	71.6	70.6	63.4
SiO_2	n.d.	n.d.	n.d.	n.d.	n.d.	3.6
CaO	0.3	n.d.	n.d.	n.d.	0.2	3.5
V_2O_3	n.d.	0.3	n.d.	n.d.	0.6	n.d.
TiO_2	0.5	n.d.	n.d.	n.d.	n.d.	1.4
Cr_2O_3	0.3	n.d.	n.d.	n.d.	0.3	n.d.
FeO	0.4	n.d.	n.d.	0.6	0.8	1.8
Total	98.0	98.8	99.8	100.6	99.3	97.1
	number per formula unit					
Mg	0.97	0.97	0.99	1.00	0.96	0.86
Al	2.00	2.01	2.00	1.99	2.00	1.85
Si	n.d.	n.d.	n.d.	n.d.	n.d.	0.09
Ca	0.01	n.d.	n.d.	n.d.	0.01	0.09
V	n.d.	0.01	n.d.	n.d.	0.01	n.d.
Ti	0.01	n.d.	n.d.	n.d.	n.d.	0.03
Cr	0.00	n.d.	n.d.	n.d.	0.01	n.d.
Fe	0.00	n.d.	n.d.	0.01	0.02	0.04
O	4.00	4.00	4.00	4.00	4.00	4.00
Cation sum	2.99	2.99	3.00	3.00	2.99	2.96
Mg/(Mg + Fe)*	100	100	100	100	98	96
Mineral	melilite					
Crystal shape	lath	lath	lath	in palisade	in framboid	near rim†
MgO	8.3	10.5	6.1	9.8	4.2	0.9
Al_2O_3	15.7	9.0	20.2	10.3	26.0	35.4
SiO_2	35.0	38.3	31.4	37.6	27.7	22.7
CaO	41.1	42.3	42.6	42.1	41.1	41.6
Total	100.1	100.1	100.3	99.8	99.0	100.6
	number per formula unit					
Mg	0.56	0.71	0.41	0.67	0.29	0.06
Al	0.84	0.48	1.09	0.56	1.41	1.90
Si	1.59	1.75	1.44	1.72	1.28	1.03
Ca	2.00	2.07	2.08	2.06	2.03	2.03
O	7.00	7.00	7.00	7.00	7.00	7.00
Cation sum	4.99	5.01	5.02	5.00	5.01	5.02
Åk‡	57	76	44	71	29	6
Mineral	anorthite			fassaite		
Crystal shape	lath	blocky	irregular	lath	blocky	near rim
MgO	n.d.	n.d.	n.d.	11.6	11.0	9.2
Al_2O_3	36.6	36.5	37.4	21.0	18.5	17.4
SiO_2	42.1	42.3	41.5	40.7	41.9	38.9
CaO	21.4	21.0	20.7	25.5	25.5	25.8
TiO_2	n.d.	n.d.	n.d.	3.5	2.6	8.5
Total	100.1	99.8	99.5	102.4	99.6	99.7
	number per formula unit					
Mg	n.d.	n.d.	n.d.	0.62	0.60	0.50
Al	2.01	2.00	2.06	0.88	0.80	0.76
Si	1.96	1.97	1.94	1.45	1.53	1.43
Ca	1.07	1.05	1.04	0.97	1.00	1.02
Ti	n.d.	n.d.	n.d.	0.09	0.07	0.23
O	8.00	8.00	8.00	6.00	6.00	6.00
Cation sum	5.04	5.03	5.03	4.02	4.00	3.95

n.d. = not detected.
* mol%.
† next to the spinel ribbon.
‡ Åkermanite content.

were analyzed by automatic peak jumping at a mass resolution power of ≥6000, sufficient to completely eliminate the hydride interference at mass 17. Secondary ions were detected by an electron multiplier operated in a pulse-counting mode. The secondary ion intensities were corrected for dead time of the detection system (15.5 or 29.5 ns depending on the analytical session).

No correction was applied for matrix effects because the effects were less than analytical errors (~5‰) in this study (Ito et al., 1998). To correct instrumental mass fractionation, a Russian spinel SPU (Yurimoto et al., 1994) with known oxygen isotope ratios was used for standardization. Other analytical methods are similar to those of Yurimoto et al. (1998) and Ito et al. (1998). After the SIMS analysis, additional petrographic characterization using the SEM-EDS system was performed to check beam overlap among different minerals with the SIMS analysis spots.

3. RESULTS

3.1. Petrography and Mineral Compositions

A coarse-grained CAI fragment named TTV1-01 (3 × 2 mm in size) was found in a thick section of Vigarano (Yoshitake et al., 2001, 2002; Fig. 1). The CAI is positioned near the edge of the section. One side of the CAI is rounded, has a Wark-Lovering rim, and is the original external margin of the CAI. The other side is fragmented and comes from the interior of the original CAI. Major minerals in the CAI are spinel (~29 vol%), melilite (~10 vol%), fassaite (~50 vol%), and anorthite (~11 vol%). Melilite, fassaite, and anorthite grains are coarse-grained and intergrown with one another, indicating crystallization from liquid. The mineral abundances, grain sizes, and absence of a core-mantle structure indicate that TTV1-01 is a coarse-grained type B2 CAI. Accessory phases of the CAI are Fe-Ni metal and refractory metal nuggets containing Pt and Mo. Secondary minerals, such as Na-bearing phases, are observed only near the rim and along some cracks.

Spinel grains are relatively small (<10 μm) and are poikilitically enclosed in all other major minerals. Framboid (El Goresy, 1979) or palisade (Wark and Lovering, 1982) structures of coarser spinel (~10 μm) are commonly observed. Mg numbers (Mg/(Mg+Fe)) are 94–100 (mol%) for most spinel grains, but Mg numbers are lower (80–98) for spinel near the rim (Table 1). Enrichments in FeO are not observed in spinel near the fragmented edge of the CAI. Minor elements present in spinel are TiO_2 (<0.51 wt%), Cr_2O_3 (<0.35 wt%) and V_2O_3 (<0.61 wt%) (Table 1). Spinel grains near the rim contain higher concentrations of TiO_2 (0.0–1.4 wt%) than spinel in the center of the CAI.

Melilite is commonly lath-shaped, with dimensions of 50–100 μm in width and 80–120 μm in length. Melilite grains are coarser in the center than near the rim. Melilite usually contains many spinel grains although some melilite grains are free of spinel inclusions. Compositions of melilite range from $Åk_6$ to $Åk_{80}$, and åkermanite-rich ones are dominant (Fig. 2). Åkermanite contents tend to be enriched in the center of CAI, and the variations become large toward the rim (Fig. 3). However, melilite of the outermost side close to the Wark-Lovering rim converges to gehlenitic composition. Åkermanite contents decrease in the zones close to spinel. Melilite in the spinel palisades has compositions of $Åk_{32}$ to $Åk_{77}$, which are similar to those of lath-shaped melilite. On the other hand, melilite enclosed in spinel framboids is åkermanite-poor ($Åk_{29}$–$Åk_{46}$) (Table 1).

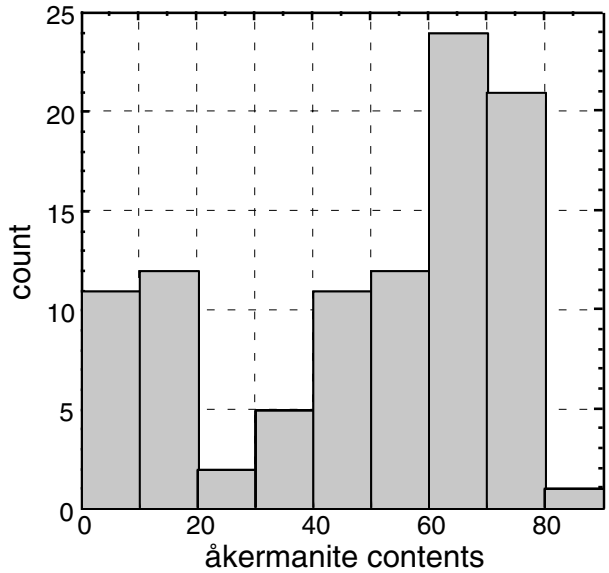

Fig. 2. Histogram of melilite compositions.

Anorthite is blocky- or lath-shaped (Fig. 4). Anorthite grains near the Wark-Lovering rim are irregularly shaped. The anorthite grains are typically 20–50 μm across with serrated grain boundaries. They commonly contain many spinel inclusions. The chemical composition is nearly pure $CaAl_2Si_2O_8$ for all crystal shapes (Table 1).

Fassaite is the most abundant phase in TTV1-01. Fassaite grains are lath- or blocky-shaped. The sizes of fassaite grains are normally 50–100 μm across, and larger grains are in the center. Fassaite commonly contains up to 21 wt% Al_2O_3 and 3.5 wt% TiO_2 (Table 1). Some fassaite grains near the rim contain high TiO_2 contents (up to 8.5 wt%).

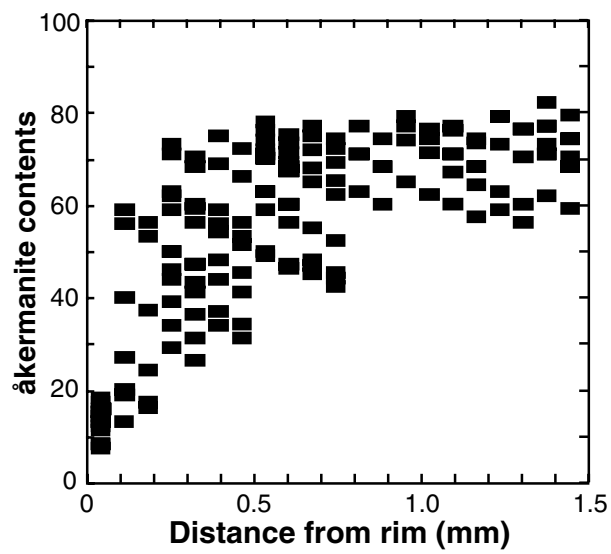

Fig. 3. Compositions of melilite grains as a function of distance from the Wark-Lovering rim. Melilite in the center is gehlenite-poor.

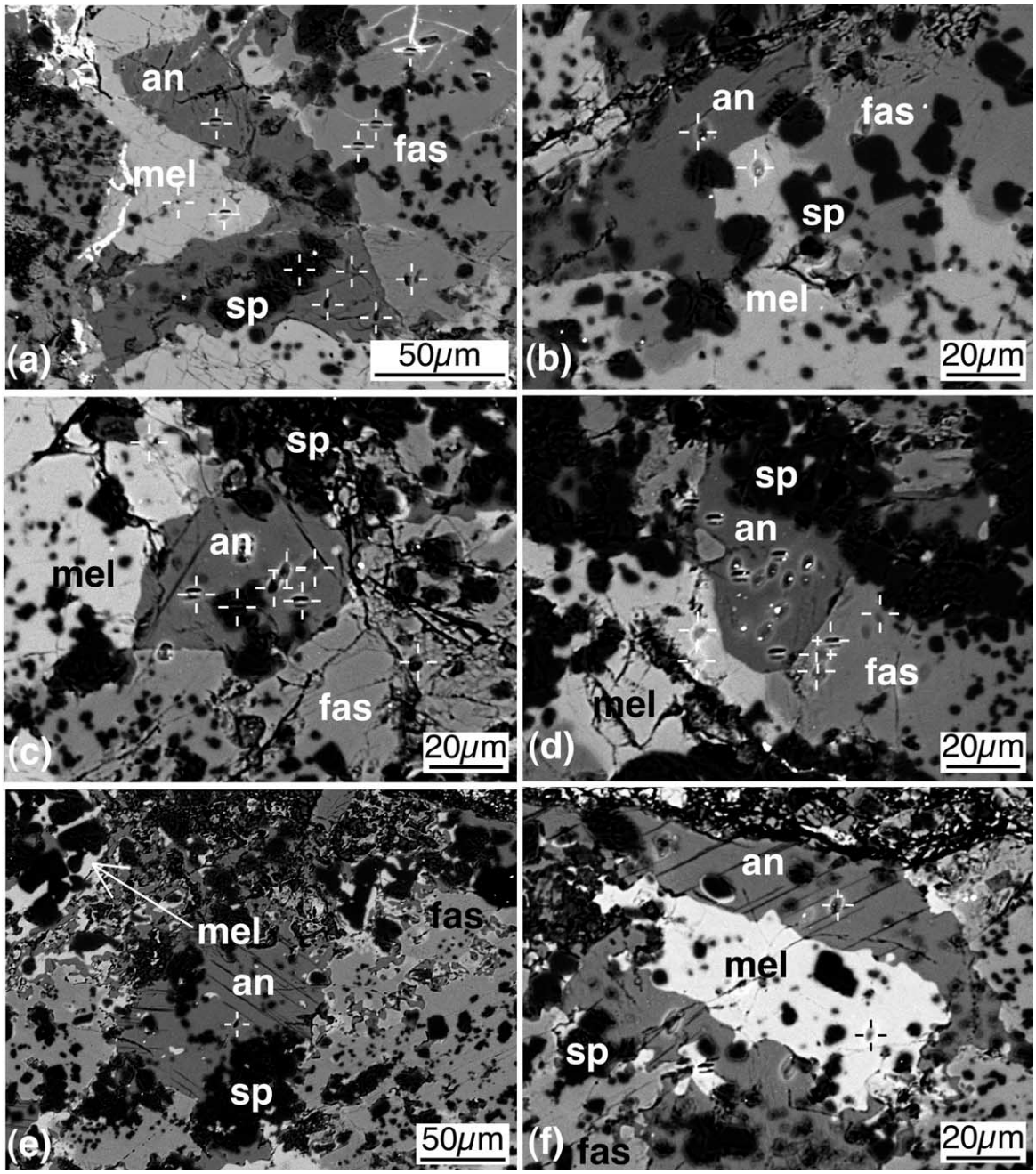

Fig. 4. Backscattered electron images of anorthite grains. We categorize anorthite grains as lath-shaped (a and b), Blocky-shaped (c and d), and irregularly shaped (e and f). Sputter craters of O-isotopic analysis are indicated by cross marks. The craters in anorthite grains of (d) are not indicated because the analyses are crowded. Positions of each figure in the CAI are shown in Figure 1. Abbreviations: sp = spinel; mel = melilite; fas = fassaite; an = anorthite.

TTV1-01 is surrounded by a Wark-Lovering rim and an accretionary rim (Figs. 1b and c). Basic layer sequences of the rim are, from inner to outer, spinel ribbon, altered layer, diopside layer, and accretionary olivine grains (Fig. 1b). This rim sequence continues to the bottom of the CAI (Fig. 1a). Melilite grains are rarely enclosed in the diopside layer (Fig. 1b) or are attached to outside of the diopside layer (Fig. 1c) with or without alteration products. The alteration products are probably decomposed melilite. Accretionary olivine grains are directly deposited on the melilite where the layer exists outside of the diopside layer (Fig. 1c). This texture suggests that these melilite grains in contact with the diopside layer are parts of the Wark-Lovering rim. The Wark-Lovering rim is sharply terminated by brecciation at the top of the CAI (Fig. 1c).

The width of the spinel ribbon is ~10 μm and the lateral

Table 2. Representative chemical compositions (weight %) of minerals in Wark-Lovering rim of TTV1-01.

	spinel ribbon			alteration layer		
Mineral	spinel	spinel	spinel	alt	diopside	diopside
Na_2O	n.d.	n.d.	n.d.	0.4	n.d.	n.d.
MgO	24.7	22.0	26.0	11.3	19.0	7.5
Al_2O_3	71.2	68.4	71.8	18.3	1.7	23.8
SiO_2	n.d.	2.3	n.d.	23.6	54.9	31.7
S	n.d.	n.d.	n.d.	5.7	n.d.	n.d.
CaO	n.d.	0.5	n.d.	19.5	23.5	25.4
V_2O_3	n.d.	n.d.	0.6	n.d.	n.d.	n.d.
TiO_2	n.d.	n.d.	0.4	n.d.	n.d.	10.5
FeO	4.8	8.6	2.5	23.1	2.4	1.6
Total	100.7	101.7	101.4	101.9	101.5	100.4
			number per formula unit			
Na	n.d.	n.d.	n.d.	0.04	n.d.	n.d.
Mg	0.89	0.79	0.92	0.79	1.01	0.41
Al	2.01	1.94	2.01	1.01	0.07	1.04
Si	n.d.	0.06	n.d.	1.10	1.96	1.18
S	n.d.	n.d.	n.d.	0.20	n.d.	n.d.
Ca	n.d.	0.01	n.d.	0.98	0.90	1.01
V	n.d.	n.d.	0.01	n.d.	n.d.	n.d.
Ti	n.d.	n.d.	0.01	n.d.	n.d.	0.29
Fe	0.10	0.17	0.05	0.90	0.07	0.05
O	4.00	4.00	4.00	7.00	6.00	6.00
Cation sum	2.99	2.97	2.98	5.02	4.01	4.00
Mg/(Mg + Fe)*	90	82	95			
	diopside layer			melilite layer		
Mineral	diopside	diopside	diopside	melilite	melilite	melilite
MgO	18.3	18.5	18.3	3.0	2.3	1.7
Al_2O_3	0.7	n.d.	1.4	31.9	33.5	32.8
SiO_2	54.1	54.7	53.7	24.4	23.5	23.8
CaO	25.6	25.0	25.9	40.2	39.7	41.1
TiO_2	n.d.	n.d.	0.3	n.d.	n.d.	n.d.
FeO	2.5	n.d.	0.8	1.5	0.7	0.5
Total	101.2	98.2	100.3	101.1	99.8	99.9
			number per formula unit			
Mg	0.98	1.01	0.99	0.20	0.16	0.12
Al	0.03	n.d.	0.06	1.71	1.81	1.77
Si	1.95	2.00	1.94	1.11	1.08	1.09
Ca	0.99	0.98	1.00	1.96	1.95	2.02
Ti	n.d.	n.d.	0.01	n.d.	n.d.	n.d.
Fe	0.08	n.d.	0.02	0.06	0.03	0.02
O	6.00	6.00	6.00	7.00	7.00	7.00
Cation sum	4.03	4.00	4.02	5.04	5.02	5.02
Åk†				20	15	12

alt = alteration products; n.d. = not detected.
* mol%.
† Åkermanite content.

continuity is not complete. The spinel ribbon of Wark-Lovering rim is in direct contact with gehlenitic melilite in the CAI. Spinel has Mg number of 82–98 with minor 0–0.4 wt% TiO_2 and 0–0.6 wt% V_2O_3 (Table 2). The Mg numbers of spinel are lower in the rim than in the CAI interior.

The alteration layer (~8 μm width) consists of very fine (~1 μm) grains, which might be altered melilite. Al-rich diopside grains (~5 μm) are often embedded in this layer. The diopside has wide ranges of Al_2O_3 (1.7–24.1 wt%), TiO_2 (0.0–10.5 wt%), and FeO (0.0–2.4 wt%) contents (Table 2).

The width of the diopside layer is ~10 μm (Fig. 5). The diopside contains small amounts of Al_2O_3 (<1.4 wt%) and TiO_2

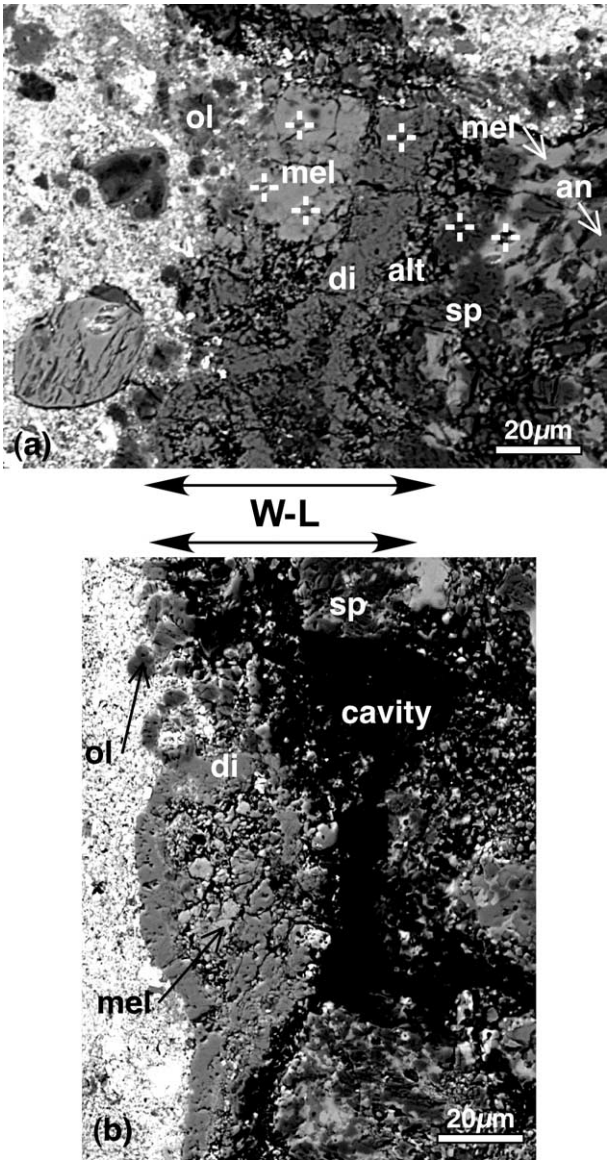

Fig. 5. Backscattered electron images of Wark-Lovering rim and accretionary rim of TTV1-01. (a) Melilite outside of diopside layer. (b) Melilite in diopside pocket. Sputtered craters of O-isotopic measurements are indicated by cross marks. Abbreviations: W-L = Wark-Lovering rim; sp = spinel; mel = melilite; alt = alteration products; di = diopside; ol = olivine; an = anorthite.

(<0.3 wt%) (Table 2). Minor amounts of FeO (<2.5 wt%) are common in the diopside. The contents of Al_2O_3 and TiO_2 are lower in this diopside than in diopside in the alteration layer and in fassaite in the CAI interior.

The melilite of the diopside layer is ≤15–20 μm. The melilite is gehlenitic (<$Åk_{20}$) and contains small amounts of FeO (1.5 wt% at the maximum) (Table 2).

The accretionary rim is dominantly composed of olivine with a range of Fo contents (Table 3). The accretionary rim is thickest in bends or pockets of the Wark-Lovering rim. Coarse-grained olivine (~10 μm) is forsteritic (>Fo_{90}), whereas fine-grained olivine (<5 μm) is fayalitic (<Fo_{70}). The fine olivine contains minor amounts of Al_2O_3 (<0.8 wt%) (Table 3). Diopside, a minor phase in the accretionary rim, contains small amounts of Al_2O_3 (<1.9 wt%), TiO_2 (<0.62 wt%), and FeO (<0.86 wt%) (Table 3).

3.2. Oxygen-Isotopic Compositions

Oxygen-isotopic compositions of minerals in TTV1-01 are listed in Tables 4, 5 and 6, and are plotted in Figures 6, 7, and 8. All of the oxygen-isotopic compositions of minerals in TTV1-01 plot along the carbonaceous chondrite anhydrous mineral (CCAM) line. We use $\delta^{18}O$ values to indicate O-isotopic compositions, because analytical errors are smaller for $\delta^{18}O$ than for $\delta^{17}O$.

3.2.1. CAI interior

Spinel and fassaite have ^{16}O-rich compositions ($\delta^{18}O$ ~−50‰–−30‰), whereas melilite is ^{16}O-poor ($\delta^{18}O$ ~0‰–15‰) (Fig. 6). The ^{16}O-poor signature of melilite is preserved in the outermost melilite crystals adjacent to the spinel ribbon of the Wark-Lovering rim (Fig. 8). No ^{16}O-rich portions have been detected in melilite grains in the interior of the CAI. A large gap is clearly observed between these compositions in Figure 8. These distinct O-isotopic distributions among minerals are commonly observed in many other coarse-grained CAIs (Clayton, 1993). On the other hand, oxygen-isotopic compositions of anorthite are distributed continuously from ^{16}O-rich to ^{16}O-poor along the CCAM line ($\delta^{18}O$ ~−40‰–5‰) (Fig. 7). The ^{16}O-rich anorthite is unusual (Fagan et al., 2004a) because anorthite in coarse-grained CAIs is commonly depleted in ^{16}O (Clayton, 1993; Kim et al., 2002). The range observed in anorthite covers the total O-isotopic variation observed in other major minerals in the CAI.

This wide distribution of O-isotopic compositions is observed not only among different anorthite grains but also within a single anorthite crystal (Fig. 7). Especially, the anorthite grain #C (Fig. 4d) shows extreme O-isotopic zoning from $\delta^{18}O$ ~−40‰ in its center to −10‰ near the edge. The zoning occurs over a distance of 10 μm. This is the first report of an anorthite single crystal having such extreme oxygen-isotopic zoning. No differences in chemical compositions or in petrographic textures are observed among anorthite grains having different ^{16}O-enrichments. Mineral assemblages and the O-isotopic characteristics of grains adjacent to anorthite are the same, irrespective of O-isotopic compositions of anorthite.

3.2.2. Wark-Lovering rim and accretionary rim

Spinel and diopside of the Wark-Lovering rim are enriched in ^{16}O, with $\delta^{18}O$ ~−45‰–−40‰ and −45‰–−35‰, respectively (Table 6; Fig. 8). These ^{16}O enrichments are similar to those of corresponding minerals observed in the interior of the CAI. We measured O-isotopic compositions in relatively large melilite grains (~20 μm) of the Wark-Lovering rim (Fig. 5). These melilite grains are enriched in ^{16}O in their centers ($\delta^{18}O$ ~−15‰), and depleted in their margins ($\delta^{18}O$ ~0‰) (Fig. 8). The ^{16}O-enrichment in the center is clearly larger than

Table 3. Representative chemical compositions (weight %) of minerals in accretionary rim.

Mineral	olivine	olivine	olivine	diopside	diopside	diopside
MgO	49.1	33.5	50.4	18.3	18.0	17.5
Al_2O_3	n.d.	0.8	n.d.	1.1	1.9	1.5
SiO_2	40.8	37.6	42.3	54.2	54.1	53.7
CaO	n.d.	0.4	n.d.	25.0	26.4	26.0
TiO_2	n.d.	n.d.	n.d.	n.d.	n.d.	0.6
FeO	9.3	27.9	7.7	0.9	0.8	n.d.
Total	99.2	100.2	100.4	99.5	101.2	99.3
			number per formula unit			
Mg	1.80	1.33	1.81	0.99	0.96	0.95
Al	n.d.	0.03	n.d.	0.05	0.08	0.07
Si	1.00	1.00	1.02	1.97	1.94	1.95
Ca	n.d.	0.01	n.d.	0.97	1.01	1.01
Ti	n.d.	n.d.	n.d.	n.d.	n.d.	0.02
Fe	0.19	0.62	0.15	0.03	0.02	n.d.
O	4.00	4.00	4.00	6.00	6.00	6.00
Cation sum	3.00	2.99	2.98	4.01	4.02	4.00
Fo*	90	68	92			

n.d. = not detected.
* Forsterite content.

those of melilite of the CAI interior but smaller than those of spinel and fassaite.

O-isotopic compositions of olivine in the accretionary rim are enriched in ^{16}O ($\delta^{18}O \sim -30‰$–$-20‰$) (Fig. 8). The small values of ^{16}O-enrichment may be due to contamination of ^{16}O-poor materials because the sputtering craters overlapped cracks in grains. Therefore it is plausible that the O-isotopic composition of accretionary olivine is $\delta^{18}O \sim -30‰$.

4. DISCUSSION

4.1. Nebular Processes

Because TTV1-01 has an igneous texture with a rounded shape, the CAI probably crystallized from a liquid droplet. Spinel is the first major liquidus mineral because the grains are poikilitically enclosed by other silicate minerals (melilite, fassaite, and anorthite). This texture is consistent with the phase relationships of cooling of CAI melts (Stolper, 1982). The ^{16}O-rich signature of spinel indicates the liquid droplet was initially enriched in ^{16}O. Occurrence of the Wark-Lovering rim and accretionary rim indicate that additional refractory minerals condensed from gas after solidification of the droplet. Condensation occurred in an ^{16}O-rich environment, because the all rim minerals, including melilite, show enrichments of ^{16}O ($\delta^{18}O = -45‰$–$-15‰$).

On the other hand, all melilite grains and some anorthite grains of the CAI interior have a ^{16}O-poor signature ($\delta^{18}O = -5‰$–$+15‰$). We must evaluate when and how such ^{16}O-poor minerals form in the interior. Grain sizes of melilite crystals are much larger in the interior (>100 μm) than in the Wark-Lovering rim (<20 μm). If O-isotopic exchange occurred after formation of the Wark-Lovering rim, the extent of O-isotopic exchange should be greater in the rim melilite than in the interior melilite because of the smaller size of the former. Therefore, ^{16}O-poor melilite must have formed before rim formation. These observations demonstrate that the O-isotopic reservoir cyclically changed from ^{16}O-rich to ^{16}O-poor and to ^{16}O-rich again. Such cycling occurred on the time scale of the formation of a single CAI.

Two kinds of mechanisms can be considered for the formation of the ^{16}O-poor interior melilite: solid-state diffusion or melting and solidification in an ^{16}O-poor environment. If diffusion is the dominant mechanism, typical diffusion distances of O isotopes are 10 μm in anorthite and more than 50 μm in melilite, based on the grain sizes. O-isotopic exchange in fassaite and spinel is negligible because the O diffusivities are more than two orders of magnitude smaller than those in anorthite and melilite (Yurimoto et al., 1989; Elphick et al., 1988; Ryerson and McKeegan, 1994). The temperature and time dependences for these diffusion distances are shown in Figure 9. Temperature ranges of 1300–1500 K and time scales of several years to several months may be consistent with these diffusion distances. The upper limit of the temperature is determined by the melting point of anorthite in a type B CAI composition (Stolper, 1982). Although O-isotopic exchange by solid-state diffusion may be applicable to this CAI, we note that O-isotopic heterogeneities among minerals in coarse-grained CAIs cannot always be interpreted by this kind of diffusion mechanism (Yurimoto et al., 1989; Yurimoto et al., 1994; Ryerson and McKeegan, 1994; Yurimoto et al., 1998).

If melting and solidification are the dominant mechanisms of O-isotopic exchange of minerals in this CAI, O-isotopic exchange towards ^{16}O-poor compositions should proceed during melting because O self-diffusion is much faster in melt than in solids. Crystals precipitated from the liquid would have different O-isotopic compositions from the relict crystals. This process has been proposed to explain an abrupt change, with a sharp boundary, of the O-isotopic distribution in a single crystal

Table 4. Oxygen isotopic compositions (‰) of spinel, melilite, and fassaite of the interior of TTV1-01.

Spot num.	Mineral	$\delta^{17}O_{SMOW}(\sigma_{mean})$	$\delta^{18}O_{SMOW}(\sigma_{mean})$
TTV1#010	spinel	−44.6 (2.4)	−48.9 (1.1)
TTV1#022	spinel	−44.1 (2.6)	−39.9 (1.2)
TTV1#032	spinel	−35.3 (2.7)	−35.1 (1.3)
TTV1#042	spinel	−52.6 (2.2)	−44.3 (1.1)
TTV1#052	spinel	−40.6 (2.7)	−36.7 (1.3)
TTV1#056	spinel	−31.7 (2.9)	−28.1 (2.3)
TTV1#058	spinel	−37.6 (2.0)	−39.0 (0.9)
TTV1#086	spinel	−49.4 (2.2)	−47.4 (1.1)
TTV1#101	spinel	−41.6 (2.5)	−32.0 (1.2)
TTV1#121	spinel	−42.8 (2.7)	−40.1 (1.1)
TTV1#004	melilite	9.7 (2.5)	16.2 (1.1)
TTV1#027	melilite	11.6 (2.0)	13.6 (0.9)
TTV1#031	melilite	3.2 (2.3)	8.0 (1.2)
TTV1#039	melilite	7.6 (2.5)	17.3 (1.5)
TTV1#053	melilite	9.8 (2.6)	15.3 (1.1)
TTV1#065	melilite	3.5 (3.6)	3.5 (1.9)
TTV1#079	melilite	2.4 (2.1)	8.5 (1.0)
TTV1#091	melilite	5.4 (2.7)	11.1 (1.0)
TTV1#095	melilite	5.4 (2.7)	8.4 (1.2)
TTV1#110	melilite	−1.7 (2.2)	3.0 (1.2)
TTV1#120	melilite	16.4 (2.2)	20.5 (1.1)
TTV1#130	melilite	9.5 (2.5)	13.2 (1.0)
TTV1#025	fassaite	−44.3 (2.3)	−41.6 (0.9)
TTV1#030	fassaite	−41.6 (2.0)	−38.1 (1.1)
TTV1#034	fassaite	−40.5 (2.1)	−34.5 (1.1)
TTV1#036	fassaite	−30.1 (2.8)	−26.7 (1.4)
TTV1#048	fassaite	−39.8 (2.3)	−33.8 (1.0)
TTV1#062	fassaite	−39.2 (2.3)	−34.9 (1.1)
TTV1#087	fassaite	−36.6 (2.4)	−35.1 (1.3)
TTV1#088	fassaite	−39.5 (2.7)	−36.7 (1.3)
TTV1#106	fassaite	−42.5 (2.3)	−36.6 (1.1)
TTV1#115	fassaite	−24.9 (2.3)	−20.2 (1.3)
TTV1#116	fassaite	−36.5 (2.0)	−29.9 (1.2)
TTV1#117	fassaite	−33.2 (2.6)	−30.9 (1.3)
TTV1#129	fassaite	−38.9 (2.0)	−35.1 (1.0)
TTV1#164	fassaite	−39.6 (2.2)	−29.2 (0.8)
TTV1#207	fassaite	−44.5 (2.2)	−45.1 (1.3)

σ_{mean} is the standard deviation of the mean determined by variation of secondary ion intensities corresponding to precisions for a series of measurements. Accuracy of δ-values (2σ) is estimated from reproducibilities of standards to be ±7.6‰ and ±5.9‰ for $\delta^{17}O$ and $\delta^{18}O$, respectively.

in a coarse-grained CAI (Yurimoto et al., 1998) and between crystals (Yurimoto et al., 1994). A serious concern of this process comes from equilibrium melting sequences of type B CAIs: fassaite (1230°C), anorthite (1260°C), melilite (1400°C), and spinel (1550°C) (Stolper, 1982). The CAI we studied shows that fassaite and some of the anorthite have ^{16}O-rich signatures, indicating that they are relict minerals if isotopic exchange occurred during a melting process. To avoid inconsistency between the equilibrium melting sequence and the O-isotopic evidence in the CAI, kinetic melting may be one of the solutions. According to the kinetic melting model (Greenwood and Hess, 1996), the melting rate is faster in melilite, followed by anorthite, and then diopside, corresponding to the ^{16}O depletions among minerals in TTV1-01.

To determine the O-isotopic exchange mechanism, observations of the gradient of the O-isotope zoning in anorthite would give important information. However, although we used a ~3-μm beam, the spatial resolution was not high enough to evaluate whether the O-isotopic zoning width of anorthite (<10 μm) resulted from solid-state diffusion or melting and overgrowth. In conclusion, the occurrence of ^{16}O-poor melilite and anorthite with ^{16}O-rich spinel, fassaite, and anorthite indicates that multiple thermal events in various O-isotopic environments are at least required. Such an astrophysical setting of CAI formation would be realized at the inner edge of the solar nebula around the protosun (Shu et al., 1997; Yurimoto et al., 2001; Itoh and Yurimoto, 2003).

4.2. Parent Body Processes

The Vigarano parent body experienced aqueous and thermal metamorphism under moderate temperatures (700–800 K) (Lee et al., 1996). The metamorphic event might have disturbed the O-isotopic distribution within ^{16}O-rich CAI minerals, because the bulk meteorite is depleted in ^{16}O.

All minerals in the Wark-Lovering rim are strongly enriched in ^{16}O ($\delta^{18}O$ ~−40‰), but the melilite in the rim is less enriched in ^{16}O ($\delta^{18}O$ ~−20‰). Moreover, the melilite rim parts are depleted in ^{16}O ($\delta^{18}O$ ~0‰) relative to their core parts. These observations suggest that the isotopic composition of the rim melilite was originally $\delta^{18}O$ ~−40‰, like other minerals in the Wark-Lovering rim and accretionary rim. The original ^{16}O-rich signatures could have been disturbed by later processes after rim formation. The O-isotopic disturbance in the melilite layer is on a scale of 10 μm (Fig. 5). Because the original texture is well preserved in the Wark-Lovering rim, the O-isotopic disturbance probably occurred in the solid state, by diffusion. The 10-μm disturbances could have been achieved in ~10^7 years at 800 K (estimated alteration temperature of the Vigarano parent-body, Lee et al., 1996) by solid-state diffusion (Fig. 9). The annealing duration may be shorter if the O-isotopic exchange rate was enhanced under aqueous conditions. Such enhancement of O-isotopic exchange in melilite has been observed in fine-grained CAIs in CO and CV chondrites (Wasson et al., 2001; Itoh et al., 2004; Fagan et al., 2002). The presence of ^{16}O-rich fine-grained melilite in the Wark-Lovering rim indicates that coarse-grained melilite in the CAI interior did not become relatively ^{16}O-poor by parent body processes such as aqueous or thermal metamorphism.

It is notable that many of the ^{16}O-poor melilite grains in the CAI interior appear to be heavier than typical bulk O-isotopic compositions for CV chondrites (Clayton and Mayeda, 1999). This provides an additional argument that the process responsible for incorporating isotopically heavy oxygen into the CAI interior occurred in the nebula rather than the parent body, because parent body processes would tend to draw the O-isotopic composition of every mineral toward the bulk value or cause them to fall along a single mass fractionation line (Young and Russell, 1998).

5. CONCLUSION

A coarse-grained type B2 CAI, TTV1-01, from the reduced CV3 Vigarano has been studied by secondary ion mass spectrometry (SIMS). Oxygen-isotopic analyses, combined with mineralogic and petrographic observations, were performed for individual minerals of the CAI interior, Wark-Lovering rim, and accretionary rim. The oxygen-isotopic compositions of minerals in TTV1-01 are distributed along the carbonaceous chondrite anhydrous mineral (CCAM) line.

In the CAI interior, spinel and fassaite are enriched in ^{16}O=($\delta^{18}O$ −50‰–−30‰) whereas melilite is relatively de-

Table 5. Oxygen isotopic compositions (‰) of anorthite in TTV1-01.

Spot num.	Mineral	Grain	$\delta^{17}O_{SMOW}$ (σ_{mean})	$\delta^{18}O_{SMOW}$ (σ_{mean})
TTV1#023	anorthite	A	−12.7 (2.8)	−4.2 (1.5)
TTV1#024	anorthite	A	−6.1 (2.2)	3.6 (1.1)
TTV1#028	anorthite	A	0.0 (2.5)	5.1 (1.3)
TTV1#118	anorthite	A	−1.8 (2.6)	1.3 (1.0)
TTV1#043	anorthite	B	−38.9 (2.2)	−36.1 (0.9)
TTV1#107	anorthite	B	−34.9 (2.1)	−33.5 (1.2)
TTV1#108	anorthite	B	−39.8 (2.5)	−41.4 (0.9)
TTV1#122	anorthite	B	−37.8 (2.0)	−33.8 (1.2)
TTV1#123	anorthite	B	−35.9 (2.5)	−32.9 (1.3)
TTV1#061	anorthite	C	−32.8 (2.3)	−27.5 (1.1)
TTV1#089	anorthite	C	−30.5 (2.2)	−21.2 (0.9)
TTV1#090	anorthite	C	−31.7 (2.1)	−24.9 (1.1)
TTV1#093	anorthite	C	−37.5 (2.3)	−34.7 (1.0)
TTV1#102	anorthite	C	−39.2 (2.5)	−35.2 (1.0)
TTV1#103	anorthite	C	−40.9 (2.2)	−35.1 (1.3)
TTV1#104	anorthite	C	−38.1 (2.5)	−37.3 (1.0)
TTV1#105	anorthite	C	−12.2 (2.5)	0.2 (1.4)
TTV1#125	anorthite	C	−15.8 (2.3)	−14.4 (1.1)
TTV1#126	anorthite	C	−20.3 (2.3)	−17.3 (1.1)
TTV1#127	anorthite	C	−32.5 (2.5)	−28.6 (1.1)
TTV1#128	anorthite	C	−23.5 (2.5)	−19.3 (1.1)
TTV1#041	anorthite	D	−13.1 (2.1)	−6.5 (1.2)
TTV1#083	anorthite	D	−11.3 (2.4)	−8.4 (0.9)
TTV1#085	anorthite	D	−12.8 (2.6)	−7.2 (1.1)
TTV1#131	anorthite	D	−20.1 (2.8)	−19.4 (1.1)
TTV1#162	anorthite	E	−10.6 (2.2)	2.7 (1.2)
TTV1#163	anorthite	E	−9.7 (2.6)	4.7 (1.2)
TTV1#167	anorthite	E	−44.7 (2.5)	−42.2 (1.1)
TTV1#072	anorthite	F	−37.5 (3.0)	−25.3 (1.7)
TTV1#078	anorthite	G	−39.5 (2.8)	−43.3 (1.2)
TTV1#109	anorthite	H	−29.8 (2.1)	−32.4 (1.0)
TTV1#156	anorthite	I	−40.0 (2.3)	−38.7 (1.5)
TTV1#158	anorthite	I	−44.8 (2.6)	−38.4 (1.6)

Backscatterd electron images of anorthite grains A, B, C, F, G, and H are shown in Fig. 4a, c, d, b, e, and f, respectively. σ_{mean} is the standard deviation of the mean determined by variation of secondary ion intensities corresponding to precisions for a series of measurements. Accuracy of δ-values is estimated from reproducibilities of standards to be ±7.6‰ and ±5.9‰ for $\delta^{17}O$ and $\delta^{18}O$, respectively.

pleted in ^{16}O=($\delta^{18}O$ 0‰–+15‰). Oxygen-isotopic compositions of anorthite are distributed continuously from ^{16}O-rich ($\delta^{18}O$ ∼−40‰) to ^{16}O-poor ($\delta^{18}O$ ∼+5‰) values along CCAM. The range observed in anorthite covers O-isotopic variations observed among other major minerals in the CAI. Such extreme O-isotopic variations have been also observed not only among different crystals but within single anorthite crystals. The intracrystalline isotopic zoning trend is from ^{16}O-rich in the centers of grains ($\delta^{18}O$ ∼−40‰) to ^{16}O-poor ($\delta^{18}O$ ∼−15‰) near the rim.

Spinel and diopside of the Wark-Lovering rim are enriched in ^{16}O ($\delta^{18}O$ ∼−40‰). The melilite in the Wark-Lovering rim is relatively enriched in ^{16}O ($\delta^{18}O$ ∼−15‰) in its center and is depleted in ^{16}O ($\delta^{18}O$ ∼0‰) at its margin. The O-isotopic composition of olivine in the accretionary rim is also enriched in ^{16}O ($\delta^{18}O$ ∼−30‰).

The O-isotopic composition of melilite in the Wark-Lovering rim was originally enriched in ^{16}O, comparable to other minerals in the rim ($\delta^{18}O$ ∼−40‰), and changed to the present values probably on the parent body. However, the O-isotopic compositions of coarse-grained melilite in the CAI interior cannot be accounted for this diffusion process.

An intergrown texture of coarse-grained crystals and a rounded outer shape suggests that CAI interior crystallized from a liquid droplet. However, the heterogeneous O-isotopic

Table 6. Oxygen isotopic compositions (‰) of minerals around Wark-Lovering rim of TTV1-01.

Spot num.	Mineral	$\delta^{17}O_{SMOW}$ (σ_{mean})	$\delta^{18}O_{SMOW}$ (σ_{mean})	Fo**
TTV1#139	melilite*	−5.1 (2.2)	6.5 (1.1)	
TTV1#140	melilite*	−3.0 (2.6)	4.1 (1.1)	
TTV1#146	melilite*	10.9 (2.6)	16.4 (1.4)	
TTV1#193	melilite*	−3.6 (2.2)	−4.0 (1.5)	
TTV1#194	melilite*	3.5 (2.3)	10.5 (1.0)	
TTV1#144	spinel†	−46.6 (2.2)	−43.1 (1.3)	
TTV1#208	spinel†	−44.2 (2.4)	−47.4 (1.3)	
TTV1#135	diopside†	−41.7 (2.1)	−42.7 (1.1)	
TTV1#151	diopside†	−34.9 (2.5)	−36.3 (1.3)	
TTV1#134	melilite†	−18.0 (2.0)	−16.9 (1.1)	
TTV1#142	melilite†	0.5 (2.6)	−2.4 (1.4)	
TTV1#143	melilite†	−17.1 (2.2)	−14.1 (1.2)	
TTV1#190	olivine‡	−37.2 (1.8)	−33.8 (1.1)	84
TTV1#192	olivine‡,#	−20.4 (2.9)	−20.1 (1.6)	86
TTV1#195	olivine‡,#	−22.4 (2.2)	−17.4 (1.5)	86

σ_{mean} is the standard deviation of the mean determined by variation of secondary ion intensities corresponding to precisions for a series of measurements. Accuracy of δ-values is estimated from reproducibilities of standards to be ±7.6‰ and ±5.9‰ for $\delta^{17}O$ and $\delta^{18}O$, respectively.

* CAI interior next to spinel ribbon.

† Wark-Lovering rim.

‡ Accretionary rim.

\# Included cracks.

** Forsterite content.

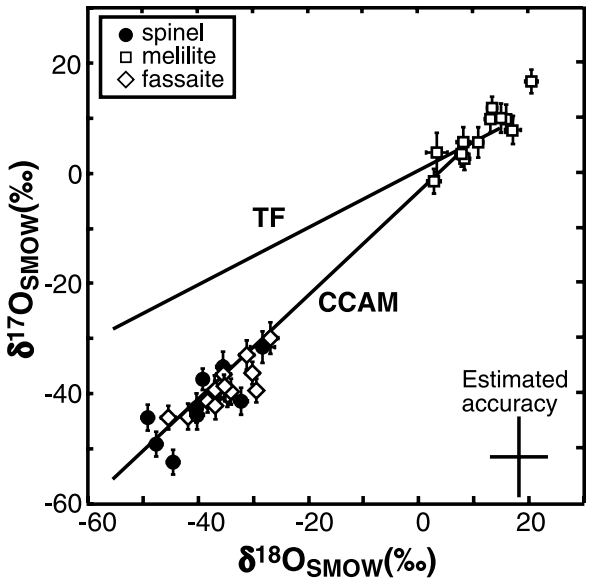

Fig. 6. Oxygen-isotopic compositions of spinel, fassaite, and melilite of CAI interior of TTV1-01. All data are distributed along the CCAM line. Spinel and fassaite are ^{16}O-rich, whereas melilite is ^{16}O-poor. TF = terrestrial fractionation line; CCAM = carbonaceous chondrite anhydrous mineral line. Error bars of each analysis show standard errors. Estimated total accuracy (2σ) is also shown.

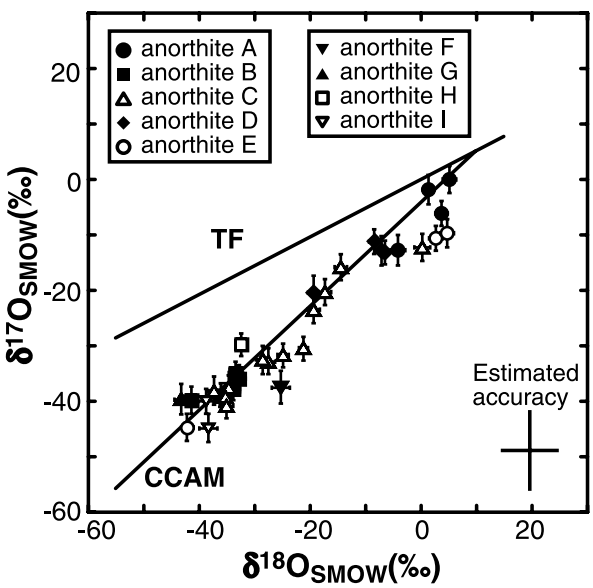

Fig. 7. Oxygen-isotopic compositions of anorthite in TTV1-01. Different symbol is used for each anorthite single crystal. Error bars of each analysis show standard errors. Estimated total accuracy (2σ) is also shown.

distribution among minerals and within anorthite requires multiple heating events in different O-isotopic environments. The O-isotopic exchange of melilite in the CAI interior must have occurred before Wark-Lovering rim formation. Two exchange mechanisms in the solar nebula (solid-state diffusion vs. kinetic melting and solidification) can be considered to interpret the observations. Further high-resolution measurements of O-isotopic zoning of anorthite would be required to determine the

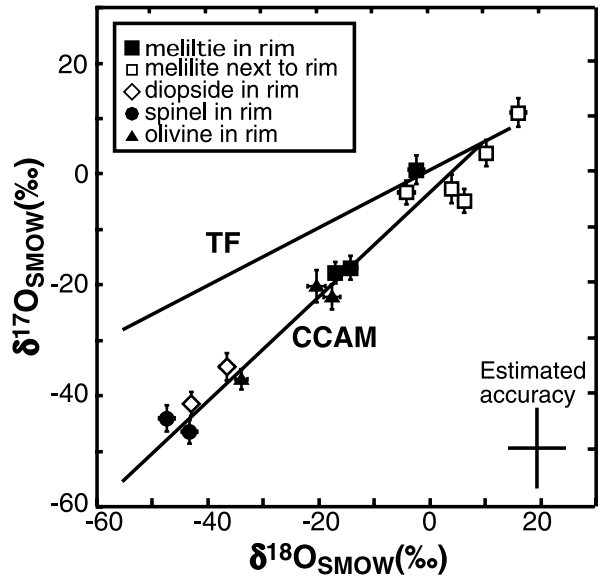

Fig. 8. Oxygen-isotopic compositions of individual minerals around Wark-Lovering rim of TTV1-01. Error bars of each analysis show standard errors. Estimated total accuracy (2σ) is also shown.

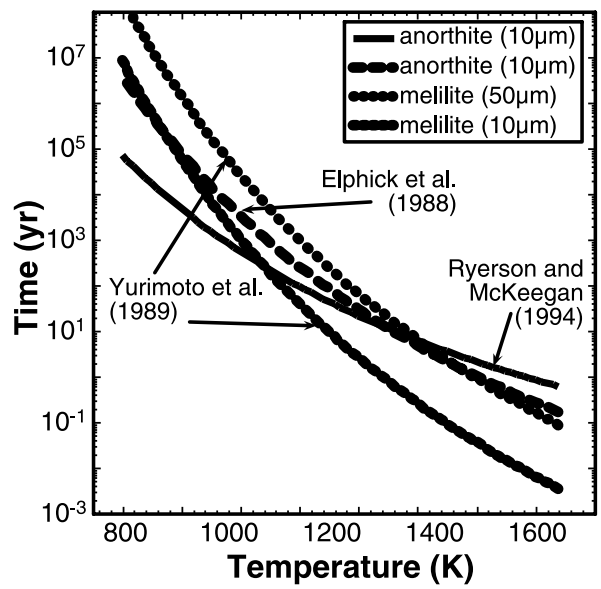

Fig. 9. Temperature and time dependences for diffusion distances of oxygen. The diffusion distances in minerals are shown in the legend.

mechanism. After the O-isotopic exchange of CAI interior, ^{16}O-rich refractory minerals condensed from gas to form the Wark-Lovering rim and accretionary rim. These observations demonstrate that the O-isotopic environment in the nebula cyclically changed at least from ^{16}O-rich to ^{16}O-poor and to ^{16}O-rich within the time scale of single CAI formation.

Acknowledgments—We thank T. J. Fagan for discussion and improving the English. We also thank two anonymous reviewers for constructive comment and improving the English and S. S. Russell for thoughtful comments and editorials. This work was supported by Monka-sho grants.

Associate editor: Sara Russell

REFERENCES

Aléon J., Krot A. N., and McKeegan K. D. (2002) Calcium-aluminum–rich inclusions and amoeboid olivine aggregates from the CR carbonaceous chondrites. *Meteorit. Planet. Sci.* **37,** 1729–1755.

Ash R. D. and Young E. D. (2000) Clarity and confusion: The history of Allende chondrules as evinced by oxygen isotopes. *Lunar Planet. Sci. XXXI* Lunar Planet. Inst., Houston. #1881 (abstr.).

Clayton R. N. (1993) Oxygen isotopes in meteorites. *Ann. Rev. Earth Planet. Sci. Lett.* **21,** 115–149.

Clayton R. N. (2002) Solar system: Self-shielding in the solar nebula. *Nature* **402,** 860–861.

Clayton R. N. and Mayeda T. K. (1999) Oxygen isotope studies of carbonaceous chondrites. *Geochim. Cosmochim. Acta* **63,** 2089–2104.

Cosarinsky M., Leshin L. A., MacPherson G. J., and Guan Y. (2001) Fine-grained rims around calcium-aluminum–rich inclusions in the Vigarano and Allende CV chondrites: Petrography and oxygen isotopic composition. *Meteorit. Planet. Sci.* **36,** A44 (abstr).

Cosarinsky M., Leshin L. A., MacPherson G. J., Krot A. N., and Guan Y (2002) Oxygen isotopic composition of olivines from matrices and accretionary rims around Ca-Al–rich inclusions in CV chondrites [abstract]. *Meteorit. Planet. Sci.* **37,** A38.

El Goresy A., Nagel K., and Ramdohr P. (1979) Spinel framboids and fremdlinge in Allende inclusion: Possible sequential markers in the early solar system. *Proc. 10th Lunar Planet. Sci. Conf.* 833–850.

Elphick S. C., Graham C. M., and Dennis P. F. (1988) An ion microprobe study of anhydrous oxygen diffusion in anorthite, a comparison with hydrothermal data and some geological implications. *Contrib. mineral. petrol.* **100,** 490–495.

Fagan T. J., Yurimoto H., Krot A. N., and Keil K. (2002) Constraints on oxygen isotopic evolution from an amoeboid olivine aggregate and Ca, Al–rich inclusion from the CV3 Efremovka. *Lunar Planet. Sci. XXXIII.* Lunar Planet. Inst., Houston. #1507 (abstr.).

Fagan T. J., Krot A. N., Keil K., and Yurimoto H. (2004a) Oxygen isotopic alteration of Ca-Al–rich inclusions from Efremovka: Nebular or parent-body setting. *Meteorit. Planet. Sci.* **39,** 1257–1272.

Fagan T. J., Krot A. N., Keil K., and Yurimoto H. (2004b) Oxygen isotopic evolution of amoeboid olivine aggregates in the reduced CV3 chondrites Efremovka, Vigarano and Leoville. *Geochim. Cosmochim. Acta* **68,** 2591–2611.

Greenwood J. P., and Hess P. C. (1996) Congruent melting kinetics, constraints on chondrule formation. In *Chondrules and the Protoplanetary Disk* (eds. R. H. Jones and E. R. D. Scott), pp. 205–211. Cambridge University Press.

Hiyagon H (1998) Distribution of oxygen isotopes in and around some refractory inclusions from Allende. *Lunar Planet. Sci. XXIX.* Lunar Planet. Inst., Houston. #1582 (abstr.).

Imai H. and Yurimoto H. (2003) Oxygen isotopic distribution in an amoeboid olivine aggregate from the Allende CV chondrite: Primary and secondary processes. *Geochim. Cosmochim. Acta* **67,** 765–772.

Ito M., Yurimoto H., and Nagasawa H. (1998) Oxygen isotope microanalysis of CAI by SIMS: an evidence for isotopically anomalous melilite. *Lunar Planet. Sci. XXIX.* Lunar Planet. Inst., Houston. #1556 (abstr.).

Itoh S., and Yurimoto H. (2003) Contemporaneous formation of chondrules and refractory inclusions in the early solar system. *Nature* **423,** 728–731.

Itoh S., Kojima H., and Yurimoto H. (2004) Petrography and oxygen isotopic compositions in refractory inclusions from CO chondrites. *Geochim. Cosmochim. Acta* **68,** 183–194.

Kim G. L., Yurimoto H., and Sueno S. (2002) Oxygen isotopic composition of a compound Ca-Al-rich inclusion from Allende meteorite: Implications for origin of palisade bodies and O-isotopic environment in the CAI forming region. *J. Mineral. Petrol. Sci.* **97,** 161–167.

Kitamura Y. and Shimizu M. (1983) Oxygen isotopic anomaly and solar nebular photochemistry. *Moon Planet* **29,** 199–202.

Kobayashi S., Imai H., and Yurimoto H. (2003) New extreme ^{16}O-rich reservoir in the early solar system. *Geochem. J.* **37,** 663–669.

Krot A. N., Meibom A., and Keil K. (2000) A clast of Bali-like oxidized CV material in the reduced CV chondrite breccia Vigarano. *Meteorit. Planet. Sci.* **35,** 817–825.

Krot A. N., McKeegan K. D., Leshin L. A., MacPherson G. J., and Scott E. R. D. (2002) Existence of an ^{16}O-rich gaseous reservoir in the solar nebula. *Science* **295,** 1051–1054.

Lee M. R., Hutchison R., and Graham A. (1996) Aqueous alteration in the matrix of the Vigarano (CV3) carbonaceous chondrite. *Meteorit. Planet. Sci.* **31,** 477–483.

Lyons J. R., and Young E. D. (2004) Evolution of oxygen isotopes in the solar nebula. *Lunar Planet. Sci. XXXV.* Lunar Planet. Inst., Houston. #1970 (abstr.).

McKeegan K. D., Leshin L. A., and MacPherson G. J. (1998) Oxygen-isotope stratigraphy a Vigarano type A calcium-aluminum–rich inclusion. *Meteorit. Planet. Sci.* **33,** A102-A103 (abstr.).

Messenger S., Keller L. P., Stadermann F. J., Walker R. M., and Zinner E. (2003) Samples of stars beyond the solar system: silicate grains in interplanetary dust. *Science* **300,** 105–108.

Nagashima K., Krot A. N., and Yurimoto H. (2004) Stardust silicates from primitive meteorites. *Nature* **428,** 921–924.

Nguyen A. N., and Zinner E. (2004) Discovery of ancient silicate stardust in a meteorite. *Science* **303,** 1496–1499.

Nittler L. R. (2003) Presolar stardust in meteorites: recent advances and scientific frontiers. *Earth Planet. Sci. Lett.* **209,** 259–273.

Ryerson F. J., and McKeegan K. D. (1994) Determination of oxygen self-diffusion in åkermanite, anorthite, diopside and spinel. Implications for oxygen isotopic anomalies and the thermal histories of Ca-Al–rich inclusions. *Geochim. Cosmochim. Acta* **58,** 3713–3734.

Shu F. H., Shang H., Glassgold A. E., and Lee T. (1997) X-rays and fluctuating X-winds from protostars. *Science* **277,** 1475–1479.

Stolper E. (1982) Crystallization sequences of Ca-Al–rich inclusions from Allende: An experimental study. *Geochim. Cosmochim. Acta* **46,** 2159–2180.

Thiemens M. H. (1999) Mass-independent isotope effects in planetary atmospheres and the early solar system. *Science* **283,** 341–345.

Thiemens M. H. and Heidenreich J. E. III (1983) The mass-independent fractionation of oxygen—A novel isotope effect and its possible cosmochemical implications. *Science* **219,** 1073–1075.

Wark D. A. and Lovering J. F. (1977) Marker events in the early evolution of the solar system: Evidence from rims on Ca-Al–rich inclusions in carbonaceous chondrites. *Proc. Lunar Sci. Conf.*, **8,** 95–112.

Wark D. A., and Lovering J. F. (1982) The nature and origin of type B1 and B2 Ca-Al–rich inclusions in the Allende meteorite. *Geochim. Cosmochim. Acta* **46,** 2581–2594.

Wasson J. T., Yurimoto H., and Russell S. S. (2001) ^{16}O-rich melilite in CO3.0 chondrites: Possible formation of common, ^{16}O-poor melilite by aqueous alteration. *Geochim. Cosmochim. Acta* **65,** 4539–4549.

Yoshitake M., Koide Y., and Yurimoto H (2001) Distribution of O isotopes in a type B2 CAI from the Vigarano meteorite [abstract]. *Meteorit. Planet. Sci.* **36,** A229–A230.

Yoshitake M., Koide Y., and Yurimoto H. (2002) Distribution of O isotopes in Wark-Lovering rim of type B2 CAI from the Vigarano meteorite. *Lunar Planet. Sci. XXXIII.* Lunar Planet. Inst., Houston. #1502 (abstr.).

Young E. D. and Russell S. S. (1998) Oxygen reservoirs in the early solar nebula inferred from an Allende CAI. *Science* **282,** 452–455.

Yurimoto H. and Kuramoto K (2002) A possible scenario introducing heterogeneous oxygen isotopic distribution in proto-planetary disks [abstract]. *Meteorit. Planet. Sci.* **37,** A153.

Yurimoto H. and Kuramoto K. (2004) Molecular cloud origin for the oxygen isotope heterogeneity in the solar system. *Science* **305,** 1763–1766.

Yurimoto H., Morioka M., and Nagasawa H. (1989) Diffusion in single crystals of melilite: I. Oxygen. *Geochim. Cosmochim. Acta* **53,** 2387–2394.

Yurimoto H., Ito M., and Nagasawa H. (1998) Oxygen isotope exchange between refractory inclusion in Allende and solar nebula gas. *Science* **282,** 1874–1877.

Yurimoto H., Asada Y., and Hirai K (2001) Oxygen isotopic composition of fine-grained CAIs and genetic relation to coarse-grained CAIs [abstract]. *Meteorit. Planet. Sci.* **36,** A230.

Yurimoto H., Nagasawa H., Mori Y., and Matsubaya O. (1994) Microdistribution of oxygen isotopes in a refractory inclusion from the Allende meteorite. *Earth Planet. Sci. Lett.* **128,** 47–53.